ACS OMEGA

http://pubs.acs.org/journal/acsodf

Article

Iodine and Carbonate Species Monitoring in Molten NaOH–KOH Eutectic Scrubber via Dual-Phase *In Situ* Raman Spectroscopy

Adan Schafer Medina, Heather M. Felmy, Molly E. Vitale-Sullivan, Hope E. Lackey, Shirmir D. Branch, Samuel A. Bryan,* and Amanda M. Lines*

Cite This: *ACS Omega* 2022, 7, 40456–40465

Read Online

ACCESS | Metrics & More | Article Recommendations

ABSTRACT: Molten hydroxide scrubbing of off-gas vapors is a potential process to improve safety during the operation of generation IV molten salt nuclear reactors (MSRs). MSRs produce off-gases that can be vented by the reactor core and treated via off-gas scrubbers. Molten hydroxide scrubbers focus on capturing volatile iodine radionuclides, and they can also be used to capture aerosols and particulates and to neutralize acidic species. The performance of these scrubbers depends on the chemical interactions of the scrubbing medium with the off-gas species. Knowledge of the concentration and speciation of scrubbed or target species, as well as process and environmental interferents, can enable advanced operation of MSR off-gas treatment systems. Optical online monitoring is an excellent technology to provide this information in real time, while limiting the need for operators to interact with radioactive samples through hands-on interrogation. Raman spectroscopy can provide crucial chemical information on the state of the molten eutectic during treatment in the molten phase, as well as the gas phase. In this work, Raman spectroscopy is used to detect iodine species, specifically iodate, in the molten phase of a NaOH–KOH eutectic and to construct a calibration curve of the Raman signal of those species. Additionally, a carbonate interferent is followed from the gas phase to the liquid phase as a basis for reaching a Raman-aided mass balance of the molten hydroxide eutectic scrubber system.

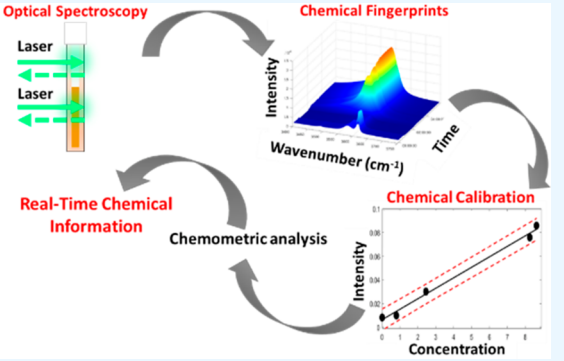

INTRODUCTION

Nuclear energy has many advantages over other renewable energy technologies, namely independence from transient conditions such as weather and location. Next-generation nuclear reactors are a promising energy source to provide stable, safe, and operationally efficient energy in an effort to decarbonize energy production.[1,2] Generation IV nuclear reactors aim to address the limitations of existing nuclear reactors and are projected to contribute significantly to many countries' baseload power in the near future.[3] Of generation IV nuclear reactor concepts, the molten salt reactor (MSR) offers several safety features, including a homogeneous fuel composition, low vapor pressures, high working temperatures at atmospheric pressure, and online refueling.[3,4] Molten salts exhibit large heat capacities, high heat transfer efficiency, high boiling points, and radiation resistance.[5−8] These physical and chemical properties contribute to the passive safety of molten salt reactor design and enable MSRs to offer several safety advantages compared to current solid-fuel reactors such as the light water reactor.

Compared to currently deployed nuclear reactor technologies, constituents of MSR off-gas streams differ in chemical speciation and fission products.[9] Off-gases from MSRs are produced by fission at the nuclear reactor core, vented from the reactor, and pumped to a series of scrubbers that selectively capture target chemical species in the off-gas stream to prevent their release into the environment.[4] Several off-gas treatment systems are being developed. These systems include solid sorbents such as silver zeolites,[10] silver mordenite,[11] silver-functionalized silica aerogels,[12] silver-loaded aluminosilicate aerogels and xerogels,[13,14] sulfur aerogels,[15] graphene aerogels,[16] metal–organic frameworks,[17] and molten salt liquid scrubbers.[10,18] More research is required to characterize each scrubber's performance in simulated and deployed treatment systems.[19] Such a characterization can be provided by online monitoring technologies. The advancement of off-gas treatment monitoring tools provides benefits beyond MSRs, including supporting applications in spent nuclear fuel pyroprocessing and waste immobilization via vitrification.[20]

Received: August 26, 2022
Accepted: October 14, 2022
Published: October 28, 2022

Overall, process monitoring tools applied to off-gas treatment processes can enable a better fundamental understanding of the process, faster optimization, and safer deployment.

MSR off-gas streams contain highly volatile radionuclides, including ^{3}H, ^{14}C, ^{85}K, and ^{129}I, that must be disposed of safely within reasonable geologic time scales.[20] Of particular interest to this work is iodine, where ^{131}I and ^{129}I can present significant biological hazards if inhaled or ingested.[20−22] Iodine-containing compounds are likely to exist in off-gases as I_2, HI, HOI, ICN, CH_3I, and ICl.[21] Ionic forms (I^-, IO_3^-) are not volatile and exist primarily in aqueous systems,[21] but they may form during the capture of the volatile iodine-containing compounds as they interact with the capturing medium. While several iodine species have already been studied for off-gas scrubbing applications,[9,11,22−27] methods to better characterize iodine scrubbing performance *in situ* and in real time are needed to better understand and optimize treatment systems.

Hydroxide-based scrubbers have been proposed as a method to capture wastes in the form of particulates, aerosols, mists, reactive gases, and residual gaseous halides.[18,19] Molten hydroxide scrubbers operate at higher temperatures compared to aqueous scrubbers, and they have been suggested to have a higher efficiency than an aqueous-based caustic scrubber.[19] This is due to the higher concentration of hydroxides available to react with incoming vapors compared to an aqueous-based caustic scrubber. The hydroxide scrubber also serves to neutralize any acidic species in the off-gas.[19] Additionally, molten hydroxide scrubbers benefit from being a nonaqueous process, which is generally an advantage for MSR subsystems (i.e., does not introduce water to the system, less cooling needed for hot off-gases). Mixed alkali hydroxide eutectics have much lower melting points than pure hydroxides and are therefore favored, such as NaOH−KOH (51:49 molar ratio; 170 °C) vs the pure component melting points (NaOH, 319 °C; KOH, 405 °C).[28−30]

Ultimately, the performance of off-gas treatment systems is a matter of chemistry, where a better understanding of speciation, kinetics, and in-melt interactions can allow for process optimization and control. Optical spectroscopy is an ideal tool for the characterization of these systems because it provides unique insight into the solution chemistry.[31−33] Furthermore, it can be deployed *in situ* for the characterization of complex chemical systems in harsh (high temperature, corrosive, hazardous) environments.[34−36]

Here, Raman spectroscopy is evaluated for the use of qualitatively determining iodine speciation. Note that ultraviolet−visible (UV−vis) detection was also integrated into the novel setup, as will be discussed in following sections, though the target species studied here did not have notable fingerprints in that optical region. This technique still presents value in the determination of when the salt is optically transparent (e.g., when it is fully melted or indicating when precipitate forms). Furthermore, the ability to quantify iodine and interferent species within the molten hydroxide salt eutectic are discussed.

This work also covers a novel demonstration of dual-phase (e.g., liquid and gas) Raman spectroscopy, which can be used to monitor targets as they transfer from one phase to another. This type of approach supports monitoring of mass balance through the off-gas treatment system and is a key method for a better understanding and optimization of the process.

EXPERIMENTAL SECTION

Materials. Chemicals purchased from Sigma-Aldrich were anhydrous where available and included sodium iodide (NaI ≥99.5%), sodium iodate ($NaIO_3$ ≥99.5%), sodium carbonate (Na_2CO_3 ≥99.5%), potassium hydroxide (KOH ≥99.95%), and sodium hydroxide (NaOH ≥97%).

Alumina tubes (0.060 in. inner diameter) and alumina rods (0.030 in. diameter) were purchased from CoorsTek. Custom square bore quartz cuvettes (15.5 cm length, 4 mm path length) were purchased from Reflex Analytical. Alumina tubes, alumina rods, and quartz cuvettes were cleaned by immersion in dilute HCl for 30 min, rinsed with 18 MΩ cm deionized water, and dried at 120 °C for 4 h prior to use. Custom cuvette caps were printed from polyvinylidene fluoride (PVDF) and designed with two holes centered on the top: one for an argon inlet line and one for the sample addition tube (Figure 1B).

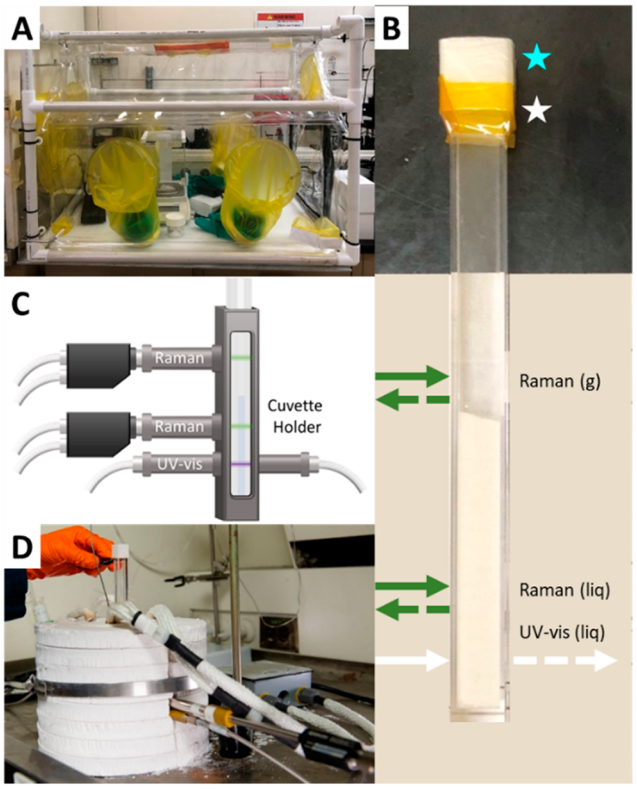

Figure 1. (A) The glovebag utilized in this work. (B) 4 mm path length quartz cuvette filled with the solid NaOH−KOH salt eutectic to a level below the gas-phase Raman beam path. An inert atmosphere was maintained with a PVDF cap, wrapped with Parafilm (cyan star), and an outer layer of polyamide heat-resistant tape (white star) protected the cuvette cap from heat. The temperature of the cuvette cap during operation did not exceed the melting point of the Parafilm (60 °C). (C) The cell holder equipped with dual liquid- and gas-phase Raman and liquid-phase UV−vis fiber optics. (D) The insulated furnace which houses the cell holder.

PVDF can be used to print an airtight cap and has a maximum use temperature of 110 °C, which is sufficient to resist the maximum temperature measured at the top of the cuvette, which was 100 °C at the maximum and usually less than 80 °C. When it was fitted to the cuvette, the exterior of the PVDF cap was less than 60 °C.

Inert Containment Practices and Sample Preparation. While great care was taken to limit the contamination of

https://doi.org/10.1021/acsomega.2c05522
ACS Omega 2022, 7, 40456−40465

the anhydrous hydroxide salts with atmospheric moisture and carbon dioxide, handling the salts outside of an atmospherically controlled glovebox for even a short time likely introduces some impurities. To address this issue, several measures were taken to reduce the impurities, including vessel cleaning strategies, reagent purification, and inert sample preparation.

NaI, $NaIO_3$, and Na_2CO_3 samples were handled and prepared in an inert glovebag filled with argon to significantly reduce the absorption of atmospheric water (Figure 1A). The argon gas was filtered through a column of desiccant before entry into the glovebag. The glovebag was sequentially inflated and deflated three times to limit moisture prior to use. Indicating Drierite was used to determine the condition of the environment in the glovebag and was generally replaced once a week. The exhaust line was routed through a mineral oil bubbler inside a fume hood as an overpressure control. Immersion of the exhaust line in several inches of mineral oil served to prevent moisture and oxygen from entering the glovebag through these ports during operation.

A 51:49 molar ratio of NaOH−KOH salts was combined by mass and ground into a homogeneous blend with an electric blender located inside the glovebag to obtain the NaOH−KOH eutectic with a melting point of 170 °C. Sodium hydroxide was dried in a vacuum oven at approximately 120 °C for >72 h, and potassium hydroxide was opened in the glovebag immediately before eutectic preparation from a vacuum-sealed glass ampule. A quartz cuvette with a 4 mm path length was filled with solid NaOH−KOH to a height of ∼3 in. The filled cuvette was capped with the PVDF cover (Figure 1B) that capped the top of the cuvette to prevent the introduction of air into the sample. The capped cuvette was placed in a cell holder inside the furnace, which was outside of the glovebag (Figure 1D), and equipped with an inlet argon line to limit the introduction of air and moisture to the hydroxide eutectic. Without the cap, moisture would immediately begin to absorb into the salt. resulting in a visible wetness.

Instrumentation. *Furnace.* The furnace was custom fabricated in-house with four identical heating coils encased in castable ceramic, with space in the center to hold the custom-made steel cell holder. The steel cell holder was made by Spectra Solutions Inc. and was equipped with fiber-optic connections for UV−vis and for dual-phase Raman probes. A dual-element thermocouple was placed into a narrow channel in the furnace adjacent to the cell holder. The sensing tip was placed in contact with the bottom Raman port. A picture of a cell being loaded into the furnace can be seen in Figure 1D.

Temperature Controller. The furnace temperature controller was a J-KEM Model 270 from J-KEM Scientific Inc., operated using the KEM Net software (v.4). An overtemperature set point of 50 °C above the maximum experiment temperature was in place as a safety measure to prevent furnace overheating. The overtemperature thermocouple was integrated with the sensing thermocouple.

Spectroscopic Instruments. The liquid-phase and gas-phase Raman spectrometers were equipped with 532 nm excitation lasers, each spectrometer was calibrated with naphthalene, and the resolution of each was ∼5 cm^{-1}. The spectrometers, lasers, and associated software and probes were purchased from Spectra Solutions Inc. (Norwood, MA, USA). The UV−vis spectrometer was equipped with LED lights (455 and 470 nm) and a halogen lamp purchased from THORLABS.

Experimental Methods. *Puck Sample Addition Method.* Sample aliquots of NaI, $NaIO_3$, and Na_2CO_3 were added to the molten NaOH−KOH using a puck sample addition method. Alumina tubes were weighed within the inert glovebag (Figure 1A). Using a small funnel, the appropriate sample was funneled into the 0.060 in. inner diameter alumina tube and packed down with an alumina rod. The resulting pucks stuck together in the tube until they were added to the melt. The mass of the filled alumina tube was recorded. Each end of the alumina tube was covered with Parafilm when it was transferred from the glovebag to the furnace. Parafilm was removed from one end of the sample tube while a 0.030 in. diameter alumina rod was inserted into the tube and the tube was inverted. The remaining Parafilm was removed from the inverted sample tube immediately before being inserted into the cuvette cap. The sample was then pushed into the molten hydroxide, the sample tube was removed, and the Parafilm was replaced on the cuvette cap. If this step was not completed quickly enough or if the tube was stored without desiccant, the powders would stick from moisture ingress, rendering them unusable. The weight difference of the alumina tube was recorded after the solid sample was delivered to the molten hydroxide salt to determine the quantity of analyte added. This process reliably delivered 98% of the solid from the tube, as determined by a preliminary trial of 10 puck additions of sodium carbonate. Because the cuvette was heating within the metal cell holder inside the furnace, it was not possible to visually observe the sample as it was being added. The long alumina tube assured that the sample was delivered directly to the molten salt rather than being inadvertently deposited on the side walls of the cuvette.

Spectroscopic Measurements. For both Raman and UV−vis spectrometers, reference spectra were collected of an empty cuvette with a 4 mm path length, a cuvette (4 mm path length) with solid NaOH−KOH, solid Na_2CO_3 in a glass scintillation vial, and solid $NaIO_3$ in a glass scintillation vial. The spectrometer integration times were set between 1 and 10 s to yield the lowest limit of detection for each spectrometer.

Raman and UV−vis spectra were collected every 20 s as the NaOH−KOH salt melted, and the spectra are shown in Figure 2B. For the solid Na_2CO_3 or solid $NaIO_3$ puck addition experiments, spectra were collected continuously after each addition.

Data Analysis Software. MATLAB (version R2020b Update 5, 9.9.0.1592791) was used for extracting and processing the Raman and UV−vis spectra.

RESULTS AND DISCUSSION

Chemistry and Chemical Targets. This work focuses on developing a process monitoring technology for the caustic NaOH−KOH molten salt eutectic environment. This system has a relatively low eutectic melting point of 170 °C. The chemical reactions of gaseous HF, HCl, and HI with liquid NaOH that are expected to occur within the molten hydroxide scrubber are proposed in Scheme 1. Sodium and potassium cations in the NaOH−KOH eutectic can react with negatively charged iodine species to form ion pairs, including NaI, $NaIO_3$, NaIO, KI, KIO_3, and KIO.[20,37]

As indicated in Scheme 1, primary iodine targets anticipated within the scrubber melt are iodate (IO_3^-) and sodium iodide (NaI). However, some literature suggests that the iodide species may transition to iodate under the conditions expected in a molten hydroxide scrubber.[19] Therefore, a primary target

https://doi.org/10.1021/acsomega.2c05522
ACS Omega 2022, 7, 40456−40465

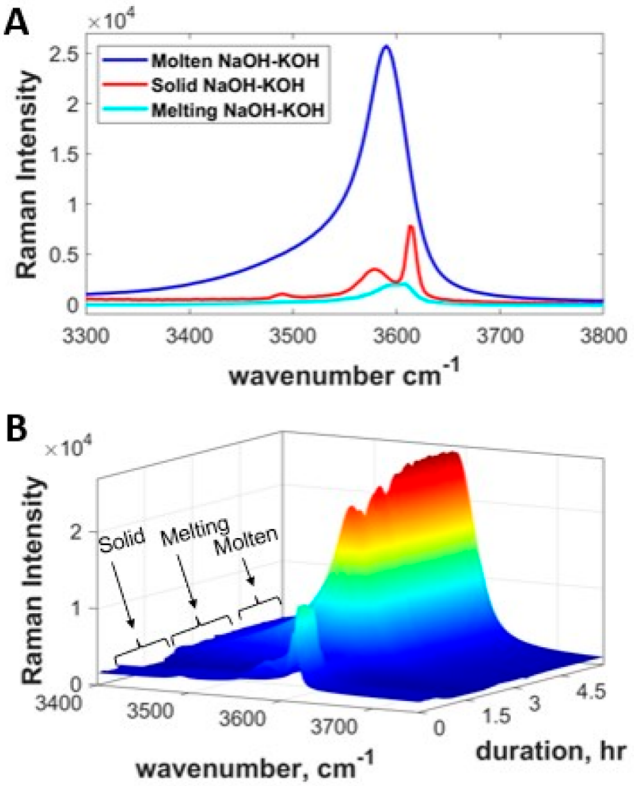

Figure 2. (A) Plots of the NaOH−KOH eutectic at three phases. (B) Three-dimensional plots of the NaOH−KOH eutectic during melting showing the two distinct peaks gradually combining and increasing in Raman intensity.

Scheme 1. Proposed Reactions of Gaseous Halides, Hydrogen Halides, and Organo-Halides with Molten Sodium Hydroxide as Described in the Literature[18,21,23,28]

$$HI_{(g)} + NaOH_{(liq)} \rightleftharpoons Na^{+}_{soln} + I^{-}_{soln} + H_2O_{(g)} \quad (1)$$

$$3I_{2(g)} + 3H_2O_{(g)} \rightarrow 5I^{-} + IO^{-}_{3\,soln} + 6H^{+}_{(soln)} \quad (2)$$

$$I_{2(g)} + H_{2(g)} + NaOH_{(liq)} \rightarrow 2Na^{+}_{soln} + 2I^{-}_{soln} + H_2O_{(g)} \quad (3)$$

$$CH_3I_{(g)} + NaOH_{(liq)} \rightarrow Na^{+}_{soln} + I^{-}_{soln} + H_2O_{(g)} + C_s + H_{2(g)} \quad (4)$$

$$4ICl_{(g)} + 2H_2O_{(g)} \rightarrow 4HCl_{(g)} + 2I_{2(g)} + O_{2(g)} \quad (5)$$

$$H_2O_{(g)} + I_{2(g)} \leftrightarrow HI_{(g)} + HOI_{(g)} \quad (6)$$

for following scrubber performance will be IO_3^-, which is known to have a unique Raman fingerprint. The I^- species is not expected to be Raman or UV−vis active but could be followed as it interacts with other species in the melt and is converted to IO_3^-. The possibility of monitoring for this will be discussed below.

It is important to note that other chemical species will be captured within the scrubber system. These can potentially interfere with the chemistry/efficient capture of iodine. Alternatively, these could interfere with monitoring of iodine targets by introducing overlapping optical fingerprints or baseline effects. A key example of this is that CO_2 is captured as CO_3^{2-} within the hydroxide melt (see Scheme 2).

Scheme 2. Proposed Reaction of Gaseous Carbon Dioxide

$$CO_{2(g)} + 2NaOH_{(liq)} \leftrightarrow 2Na^{+}_{(soln)} + CO^{2-}_{3\,(soln)} + H_2O_{(g)} \quad (7)$$

Fortunately, advanced data analysis methods suggest that optical interferents may not pose a significant challenge to spectral detection through the use of chemometric techniques such as multivariate curve resolution (MCR) analysis or partial least-squares (PLS) analysis.[32,33,39,40] However, online monitoring will be able to provide uniquely powerful insight into the chemistry of these systems. This will allow researchers and operators to understand and compensate for any deleterious impacts of dissolved interferent species.

Work presented here will focus primarily on IO_3^- dissolved in the NaOH eutectic. Some discussion will be provided regarding I^- in this same system. Monitoring of CO_3^{2-} in the melt and CO_2 in the gas phase will also be discussed.

Raman Spectra during Melting. Initial experiments focused on monitoring the chemical system as it was heated to the molten state. Figure 2A shows the Raman spectra of the solid hydroxide eutectic at room temperature, while melting, and when fully molten.

The Raman shifts of NaOH and KOH at room temperature have been reported previously to be 3632 and 3597 cm^{-1}, respectively.[41,42] However, the presence of moisture results in Raman peaks at room temperature of ∼3569 and ∼3500 cm^{-1}, respectively.[42] Therefore, the peak observed in the solid eutectic spectra at 3616 cm^{-1} is ascribed to the solid NaOH, the broad peak at 3579 cm^{-1} is ascribed to the hydrated NaOH and solid KOH combined, and the peak at 3489 cm^{-1} is ascribed to the hydrated KOH.[41] As the eutectic is heated to 200 °C, the Raman response decreases substantially (Figure 2B) before increasing and eventually merging into one broadened peak at 3590 cm^{-1}. This is similar to the values for molten NaOH (3610 cm^{-1}) and molten KOH (3607 cm^{-1}) reported by Walrafen and Douglas,[42] although they were taken at higher temperatures (427 and 409 °C, respectively).

Note that the intensity does drop during melting; this could be due to a transition from a white solid (stable Raman backscatter signal) to a highly turbid midmelt system (significant scatter and nonideal for Raman) and to an optically transparent melt (excellent Raman backscatter signal). The progression through these spectra over time can be seen in Figure 2B.

Even as an initial diagnostic, these data can be used to determine when the hydroxide melt is fully molten or when there may be variable turbidity or clarity of the melt. This can enable researchers and operators to better understand when their process is in a stable condition or possibly characterize the melting point of their system. Impurities in the stock salt can change the melting point of the mixture. It is possible that the Raman signature of the blank salt can be used as a measuring tool for when the salt is molten and provide insight into the purity of the salt or the temperature gradient in the reactor/cell.

During this melting demonstration, UV−vis was not a substantially informative diagnostic. The blank salt is optically transparent and does not have unique UV−vis fingerprints. However, UV−vis along with Raman could be used to indicate the ingrowth of a precipitate or an increase in turbidity of the salt.

https://doi.org/10.1021/acsomega.2c05522
ACS Omega 2022, 7, 40456−40465

Iodine Species Fingerprints in the NaOH−KOH Eutectic. The literature suggests that iodine could take on a variety of species within the molten eutectic.[18,19] In the molten hydroxide system, iodate is not as favored as it is an aqueous species. However, operating molten salt scrubbers will likely have some level of moisture ingress during operation or moisture production from reaction of certain species as shown in Scheme 2. Therefore, iodate was chosen as the first and primary target for this demonstration due to its polyatomic nature, making it Raman active. For these demonstrations, the NaOH−KOH salt was heated to 200 °C at a rate of 300 °C/h. When the salt was completely molten, sample additions of solid $NaIO_3$ were added to the melt using the puck addition method described previously. Raman fingerprints of the iodate species were obtained by performing a baseline normalization to the hydroxide peaks followed by a baseline correction around the iodate peaks. This change in signal due to iodate concentration is shown in Figure 3A, and the linear

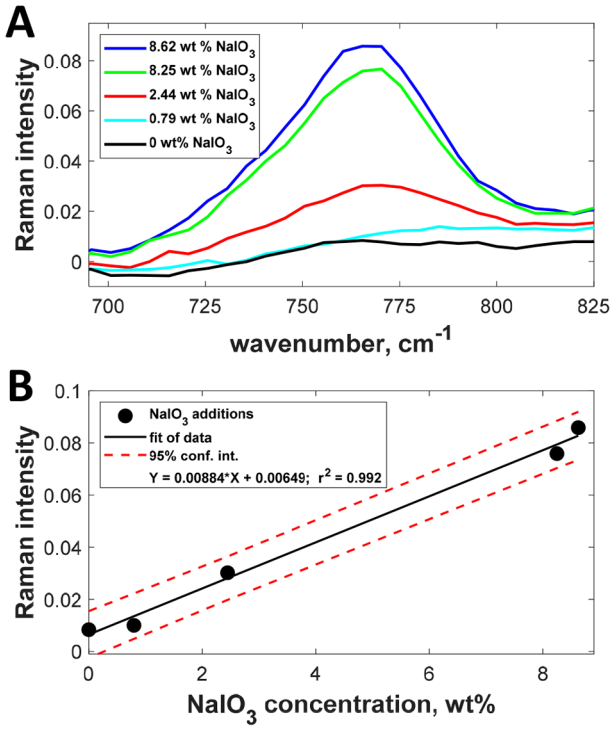

Figure 3. (A) Raman fingerprints of sodium iodate ($NaIO_3$) additions in the NaOH−KOH melt at 220 °C. Spectra were collected using a 5 s integration time, and the intensity was normalized to the OH peak at 3590 cm^{-1}. (B) Single variate calibration curve relating Raman intensity to sequential additions of solid $NaIO_3$, including the calculated 95% confidence interval of the fit of the curve.

relationship is shown in Figure 3B. The Raman peak at ~760 cm^{-1} ascribed to $NaIO_3$ is in agreement with previous reports of $NaIO_3$ in aqueous solutions as well as KIO_3 in a molten nitrate system (350 °C).[43,44]

The calibration data in Figure 3B was used to determine the limit of detection (LOD) for iodate using the equation

$$\mathrm{LOD} = \frac{3s}{m} \tag{8}$$

where s is the standard deviation of the background signal and m is the slope of the calibration curve.[45] The limit of detection was calculated to be 0.60 wt %.

Iodide is the next most likely species to be present in a molten hydroxide scrubber as identified in the literature.[38] While iodide does not have a Raman fingerprint, there was interest in seeing if iodide would convert to iodate within the melt. Following experiments of both puck addition and melting of salts directly containing iodide, no iodate fingerprints were observed to grow in, possibly due to the sparging of argon, which limited moisture and oxygen ingress. Additionally, the time frame of the experiment (~1−2 h molten) may not have allowed enough iodate to form or to be identified via Raman. There was also interest in exploring the utility of UV−vis in following these experiments. In the case of iodide, there was no color change observed but the UV−vis results did indicate an increase in turbidity from a precipitate forming shortly after addition. UV−vis along with Raman could be used to indicate the ingrowth of a precipitate or an increase in turbidity of the salt. Further investigation of this solid formation is needed to determine the nature of the precipitate. In the case of iodate, there was a yellow precipitate that may be due to an iodate species precipitating from the melt, possibly with the presence of water as well. The melt itself remained colorless during the additions, based on visual observations made when the cuvette was raised while the hydroxide was molten.

Interferent Fingerprints in the NaOH−KOH Eutectic. A major goal of this work is to demonstrate the utility of dual-phase monitoring (see the next sections). In preparation for that, a standard with a well-defined fingerprint in the salt phase and a known Raman-active counterpart in the gas phase was identified. Carbonate was chosen as this model interferent, which had the added benefit of its presence in untreated solid hydroxide salts and its contamination of purified salts from atmospheric absorption. The blank hydroxide was added to the cuvette and heated to 200 °C at a rate of 300 °C/h. The carbonate Raman peak at 1053 cm^{-1} was present prior to sodium carbonate additions, indicating that some atmospheric CO_2 was absorbed despite our best efforts at inert containment. Three sodium carbonate additions of known mass were added to the melt and their Raman intensities measured. The Raman intensities of these three additions and the original carbonate intensity (Figure 4A) were then used to make a calibration curve (Figure 4B), and a standard addition calculation was performed to back out the initial concentration of carbonate present in the salt (6.6 wt %) by using the x-axis value at a Raman intensity of zero. The standard addition method is explained in further detail elsewhere.[46] The LOD was calculated using eq 1 in Scheme 1 and determined to be 0.56 wt %.

Dual-Phase Monitoring. Following the successful demonstration of species monitoring within the NaOH−KOH eutectic melt, our research focus shifted to connecting in-salt monitoring with gas-phase monitoring. Here, technology recently utilized to characterize iodine species in the gas phase[9,23] was adapted to monitor the gas phase above the salt melt. Figure 1C includes schematics of this setup.

This combination of techniques allows for monitoring targets as they transfer from one phase to another. Demonstration of the dual-phase monitoring capability is a significant step forward and represents a highly valuable tool in the design and deployment of molten scrubber systems. Ultimately, this technique can be used to characterize the capture and loss of targets as well as maintain a material balance across a flow-through treatment system.

https://doi.org/10.1021/acsomega.2c05522
ACS Omega 2022, 7, 40456−40465

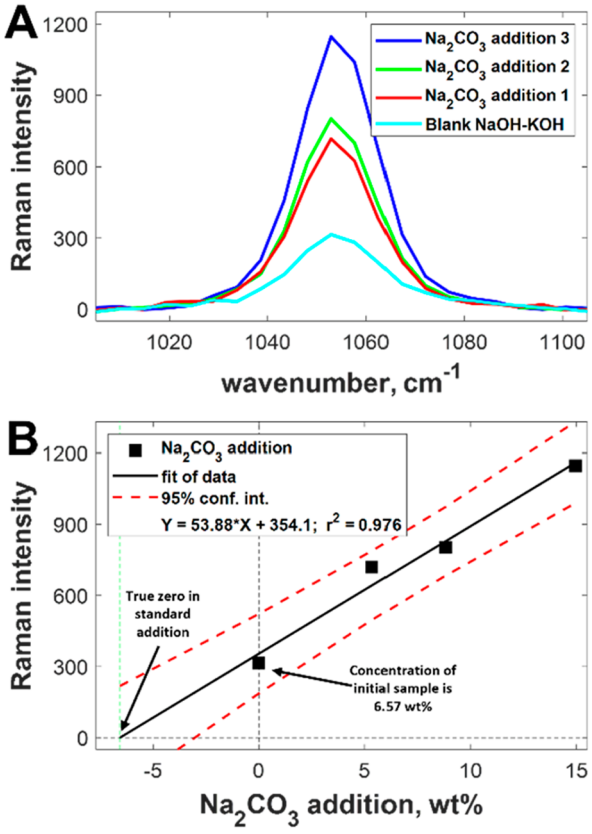

Figure 4. (A) Raman fingerprints of Na_2CO_3 added to the NaOH−KOH melt at 200 °C using a 1 s integration time. A calibration curve is shown in (B) relating the peak Raman intensity of CO_3^{2-} at 1053 cm^{-1} to the concentration of carbonate present in the melt, including the calculated 95% confidence interval of the fit of the curve.

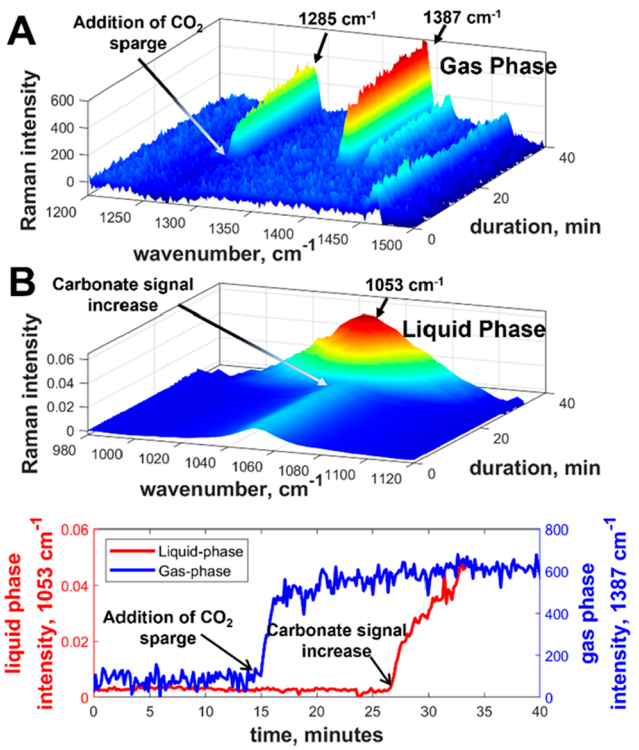

Figure 5. (A) 3D plot showing the increase of the CO_2 peaks in the gas phase as the gas line was turned on in the headspace above the molten NaOH−KOH, resulting in the ingrowth of characteristic Raman peaks at 1285 and 1387 cm^{-1} in the gas phase. Simultaneously, the liquid phase was monitored for changes in the carbonate band, as seen in (B), and the Raman intensity at 1053 and 1387 cm^{-1} are plotted in (C). The intensity of the CO_3^{2-} band at 1053 cm^{-1} increased in response to insertion of the CO_2 blanket line, showing an ingrowth of carbonate resulting from the conversion of gaseous CO_2 to the dissolved CO_3^{2-} species. The gas-phase Raman measurement leads the liquid phase by 11 $^1/_2$ min.

To support a proof-of-concept experiment, the $CO_{2(g)}$ and $CO_3^{2-}{}_{(l)}$ species were selected as the demonstration system. Again, the goal is to provide a novel demonstration of online monitoring of a known species as it transverses the gas−salt boundary. Here this involved melting a blank salt under an Ar atmosphere. After the Raman signal indicated that the system was fully melted and stable (signal matched spectra seen in Figure 2 and stable for at least 10 min), a gas stream of CO_2 was introduced into the salt cover gas. As shown in Figure 5A, the ingrowth of the CO_2 band was observed in the gas phase. Shortly thereafter, the fingerprint for CO_3^{2-} was observed to grow in the melt (see Figure 5C) as CO_2 migrated into the salt and converted to the more stable chemical form within that environment.

Real-time tracking of chemical species between the gas and liquid phases was therefore accomplished between the NaOH−KOH melt and cover gas. The CO_2 Raman bands in Figure 5A occur at 1285 and 1387 cm^{-1}, in accordance with reported CO_2 gas Raman shifts.[47] Observed CO_3^{2-} bands in Figure 5B agreed with earlier sections on this species in the salt melt. Comparing Figure 5A and Figure 5C is particularly useful in demonstrating the success of this monitoring approach, as seen by plotting the gas-phase and liquid-phase peak signals on the same plot. It indicates the ingrowth of the gas-phase bands after CO_2 is introduced to the cover gas and indicates that the delay time before the CO_3^{2-} was observed to grow in is about 10 min. In addition to enabling a fundamental characterization of the chemistry in either the gas or molten salt phase (e.g., solubility limits and diffusion kinetics) and enabling monitoring of species across phase boundaries, this type of system could be paired with flow measurements and used for mass balance analysis.

Chemometric Modeling. The Raman spectra taken during the melting process (reported in Figure 2) were analyzed further to demonstrate the utility of chemometric data analysis techniques in improving our fundamental understanding of chemical systems. Initially, a principal component analysis (PCA) was applied on the data reported in Figure 2, indicating that there were three factors providing distinct signatures. Conversely, minor shoulders are typically indicative of simple temperature-induced drift in the peaks and are therefore not considered significant signatures. Multivariate curve resolution (MCR) was then used to model the data using three factors.

MCR model factors correspond to discrete chemical signatures or "pure spectra" that are derived from the spectral signatures. In order to derive MCR factors, 100 spectra of the powdered, solid eutectic at room temperature, 100 spectra taken at the end of the heat ramp, after the eutectic was visually confirmed to be homogeneously molten, and 100 randomly selected spectra taken while the eutectic was heating were used to construct the model. The model was unconstrained and did not rely on temperature data to inform the

https://doi.org/10.1021/acsomega.2c05522
ACS Omega 2022, 7, 40456−40465

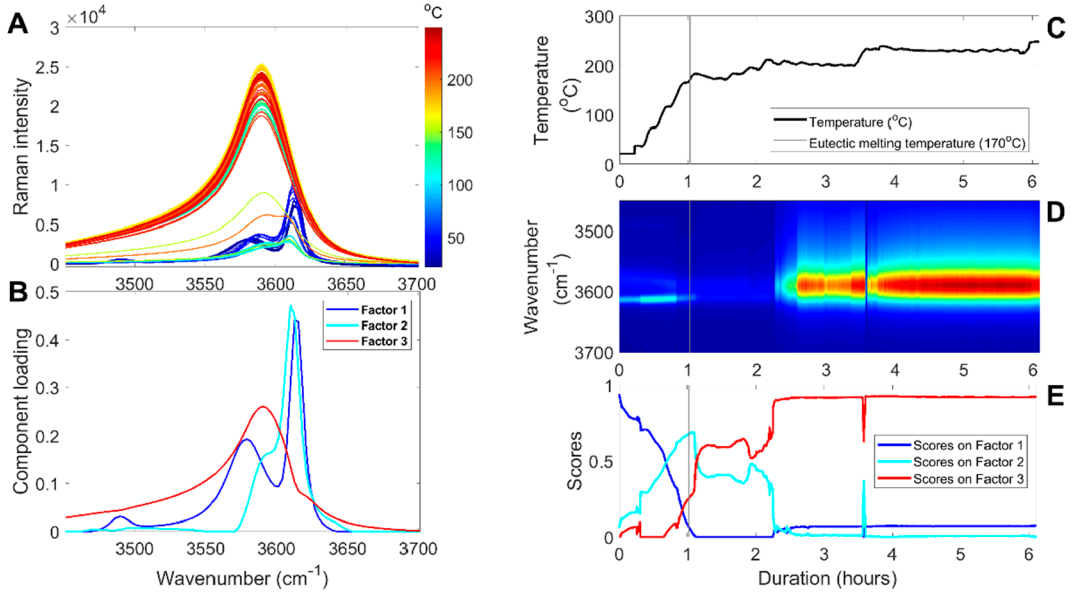

Figure 6. (A) Raman spectra of the hydroxide stretching region as the temperature of the solution increases, corrected to zero intensity in the region of 3000−3300 cm^{-1}. (B) Factors of the multivariate curve resolution (MCR) model, showing three factors that correspond to the Raman spectral signatures of the solid, melting, and molten eutectic. (C) The measured temperature near the eutectic over the duration of the experiment. (D) A top-down view of the Raman spectra over the duration of the experiment. (E) Scores of each spectra on each factor of the MCR model. The vertical gray line in (C−E) marks 170 °C, which is the expected melting point of the eutectic.

construction of the factors. Three factors were deemed significant. The results are seen in Figure 6.

Figure 6A shows spectra of the solid, powdered eutectic in dark blue, which were taken before the furnace was activated, and spectra of the molten eutectic in red and orange, which were taken after the end of the heat ramp, during which time the melt was visually confirmed to be molten with no visible solid regions remaining. Also visible are peaks that correspond to neither the solid nor the molten signature. These intermediate signatures can be seen in hours 1 to 2 in Figure 6D. Their signal is greatly decreased, relative to that of the solid signature in hour 1 and the molten signature in hours 4−6.

Each MCR factor can be seen in Figure 6B, where factors 1−3 provide distinct signatures. Factor 1, which is identical with the solid phase Raman spectrum, has peaks at 3489, 3579, and 3616 cm^{-1}. Factor 3, which is identical with the molten spectrum, has a broad peak with a maximum at 3590 cm^{-1} and a small shoulder at 3621 cm^{-1}. As can be seen in Figure 6D, the 3590 cm^{-1} peak's maximum does not significantly shift despite a change in temperature from 207 to 250 °C. Finally, factor 2 has a peak at 3610 cm^{-1} with shoulders at 3593 and 3641 cm^{-1} and a broad band between 3490 and 3550 cm^{-1}.

While it is possible that factor 2 may arise from the combination of peaks in factors 1 and 3 as they shift due to temperature, three aspects indicate that this is not the case: (1) the complete disappearance of the large 3579 cm^{-1} peak, (2) the observed stability of the 3590 cm^{-1} peak at higher temperatures, and (3) the shoulder at 3621 cm^{-1} in the molten spectra, which may arise from the solid peak at 3616 cm^{-1}, yet the sharp peak in factor 2 at 3610 cm^{-1} is lower than this shoulder. Factor 2 likely represents a combination of unique, transitory chemical and physical phenomena. An example of a physical phenomenon that might cause a unique signature is turbidity, which may occur during the conversion of discrete powdered eutectic particles to dispersed molten droplets and finally to a homogeneous melt. When they are modeled with a 2-factor model (results not shown), the results did not match known physical behaviors of the transition of a solid to a molten form. For instance, the scores on factor 1, the solid-state signature, and the scores on factor 2, the molten signature, oscillated in magnitude throughout the melt. This is incongruous with the observed, discrete signatures of solid and molten eutectic, which indicates that scores on factor 1 should go from high to low, and scores on factor two should go from low to high.

The three MCR factors were then used as hard spectral constraints in a second MCR model of all 1189 spectra taken prior to the addition of iodate or carbonate salts. Each of the 1189 spectra is decomposed into a linear combination of the three factors, much as it would be in classical least-squares. The contribution of each factor to the spectrum is quantified as a score. A higher number on a particular factor indicates that the factor explains a large amount of the variance from zero in that spectrum.

The second column of Figure 6 shows the relationship of the spectral signatures, Figure 6D, to the measured temperature in the furnace, Figure 6C, and the MCR scores, Figure 6E. As the the temperature increases up to the expected melting point of 170 °C, the spectral scores on the first MCR components gradually decrease. Concurrently, the scores on factor 2, the "melting" signature, increase. This aligns with the known behavior of solids as they are heated toward a melting point, where some solids will melt slightly before or after the observed melting point. There is a sharp break in the scores plot for factors 1 and 2 at the 1 h mark (Figure 6E) corresponding to 170 °C (Figure 6C), which aligns with the expected melting point. This indicates that the MCR model can be utilized as a means to determine the melting point of this system. After hour 1 and above 170 °C, the scores on factor 2 generally decrease while the scores on factor 3, the molten signature, generally increase. The "valley" and "plateau"

https://doi.org/10.1021/acsomega.2c05522
ACS Omega 2022, 7, 40456−40465

in factors 2 and 3, respectively, between 1.3 and 1.8 h is likely due to turbidity in the melt; as the powder melts, tiny air bubbles that were caught between solid and powder particles can remain suspended in the melt, eventually migrating up above the Raman beam path and out of the melt. The suspicion of turbidity as the cause of this incongruity is supported by the complete disappearance of factor 1 at 1.1 h and its reappearance at 2.3 h. It is unlikely that solids suddenly reformed at 2.3 h when the melt is >210 °C. It is more likely that bubbles within the melt caused the Raman signature to become very low, increasing the error in the MCR scores and making the constant, but low, contribution of the 3616 cm^{-1} peak so low as to be unmeasurable by the model. Drastic reduction in the Raman signal due to bubble-induced turbidity in solutions has been noted elsewhere.[48]

The unusual spectra at around 3.6 h in Figure 6D are likely due to cavity formation in the melt. The spike in spectral scores on factor 2 with a concomitant drop in scores on factor 1 at this time indicate that new, partially melted eutectic passed through the Raman beam path. Such occurrences have been observed in previous experiments. Due to heating gradients along the tall quartz cuvette, it has been observed that the lower portion of the eutectic becomes molten while a "crust" of solid particles remains higher in the cuvette, suspended above the molten salt, which has a lower volume (and, therefore, lower liquid level) due to the loss of air spaces between solid particles once the particles coagulate in their molten form. This can cause an argon bubble to form between the melted portion and the solid crust. Once the temperature at the level of the crust exceeds the melting temperature of the eutectic, the crust falls down into the melt, resulting in a spike of the partially melted salt's signature.

CONCLUSION

Overall, this work utilizes optical monitoring capabilities to investigate the spectroscopic signatures of IO_3^-, CO_3^{2-}, and $CO_{2(g)}$ present in and above a hydroxide molten salt eutectic of NaOH−KOH. Dual liquid- and gas-phase Raman probes enable the tracking of relevant species from one phase to another. This dual-phase monitoring approach is ideal for molten hydroxide iodine scrubbers where an off-gas waste stream travels through a liquid molten salt scrubber. Future monitoring systems can be designed to collect spectra of the off-gas stream before and after it travels through the molten hydroxide scrubber while melt-based probes can follow the capture process within the scrubber. Eventually, online monitoring systems can be deployed in industrial or commercial settings to enable operators to control and optimize off-gas treatment processes in real time. While methyl iodide would not be expected in a molten salt reactor (MSR) system, organic iodides are of concern especially in environmental or biological systems,[49] where organic substrates are available for producing methyl iodide or other organic iodide species. In the systems we are concerned with in this paper, molten salt nuclear reactors (MSRs), a ready source of organic is not available to directly form methyl iodide. For other scrubber applications, methyl iodide has been shown to be easily measured in the gas phase[50] and a suitable liquid phase[51] by Raman spectroscopy.

This represents a key advancement in process monitoring technology to support the design and deployment of off-gas treatment systems. These tools enable safe and effective treatment of hazardous reactor off-gases before release to the environment.

AUTHOR INFORMATION

Corresponding Authors

Amanda M. Lines − *Pacific Northwest National Laboratory, Richland, Washington 99354, United States*; Phone: (509) 375-5689; Email: amanda.lines@pnnl.gov

Samuel A. Bryan − *Pacific Northwest National Laboratory, Richland, Washington 99354, United States*; orcid.org/0000-0002-8826-0880; Phone: 509-375-5648; Email: sam.bryan@pnnl.gov

Authors

Adan Schafer Medina − *Pacific Northwest National Laboratory, Richland, Washington 99354, United States*

Heather M. Felmy − *Pacific Northwest National Laboratory, Richland, Washington 99354, United States*; orcid.org/0000-0002-2548-7690

Molly E. Vitale-Sullivan − *Pacific Northwest National Laboratory, Richland, Washington 99354, United States*

Hope E. Lackey − *Pacific Northwest National Laboratory, Richland, Washington 99354, United States*

Shirmir D. Branch − *Pacific Northwest National Laboratory, Richland, Washington 99354, United States*

Complete contact information is available at: https://pubs.acs.org/10.1021/acsomega.2c05522

Author Contributions

The manuscript was written through contributions of all authors. All authors have given approval to the final version of the manuscript.

Notes

The authors declare no competing financial interest.

ACKNOWLEDGMENTS

This research was supported by the U.S. Department of Energy, Office of Nuclear Energy, through the Advanced Reactor Technology Program and was performed at Pacific Northwest National Laboratory (PNNL) operated by Battelle for the U.S. Department of Energy under contract DE-AC05-76RL01830. This work was supported in part by the U.S. Department of Energy, Office of Science, Office of Workforce Development for Teachers and Scientists (WDTS) under the Science Undergraduate Laboratory Internship (SULI) program.

REFERENCES

(1) Beierschmitt, K. *Basic Research Needs for Future Nuclear Energy*; Oak Ridge National Laboratory: Report of the Basic Energy Sciences Workshop, August 9−11, 2017.

(2) Williams, D. F. B. *Molten Salt Chemistry Workshop*; Oak Ridge Naitonal Laboratory: Technology and Applied R&D Needs for Molten Salt Chemistry, April 10−12, 2017.

(3) Locatelli, G.; Mancini, M.; Todeschini, N. Generation IV nuclear reactors: Current status and future prospects. *Energy Policy* **2013**, *61*, 1503−1520.

(4) Riley, B. J.; McFarlane, J.; DelCul, G. D.; Vienna, J. D.; Contescu, C. I.; Forsberg, C. W. Molten salt reactor waste and effluent management strategies: A review. *Nucl. Eng. Des.* **2019**, *345*, 94−109.

(5) Grimes, W. R. Molten-Salt Reactor Chemistry. *Nuclear Applications and Technology* **1970**, *8* (2), 137−155.

(6) Forsberg, C. W. *Reactors with molten salts: options and missions*. Frederick Joliot & Otto Hahn Summer School on Nuclear Reactors, Physics and Fuels Systems, Cadarache, France, 2004.
(7) Serrano-López, R.; Fradera, J.; Cuesta-López, S. Molten salts database for energy applications. *Chemical Engineering and Processing: Process Intensification* **2013**, *73*, 87−102.
(8) Zhang, J. Impurities in Primary Coolant Salt of FHRs: Chemistry, Impact, and Removal Methods. *Energy Technology* **2019**, *7* (10), 1900016.
(9) Felmy, H. M.; Clifford, A. J.; Medina, A. S.; Cox, R. M.; Wilson, J. M.; Lines, A. M.; Bryan, S. A. On-Line Monitoring of Gas-Phase Molecular Iodine Using Raman and Fluorescence Spectroscopy Paired with Chemometric Analysis. *Environ. Sci. Technol.* **2021**, *55* (6), 3898−3908.
(10) Soelberg, N. R.; Garn, T. G.; Greenhalgh, M. R.; Law, J. D.; Jubin, R.; Strachan, D. M.; Thallapally, P. K. Radioactive Iodine and Krypton Control for Nuclear Fuel Reprocessing Facilities. *Sci. Technol. Nucl. Ins* **2013**, *2013*, 1−12.
(11) Wiechert, A. I.; Ladshaw, A. P.; Moon, J.; Abney, C. W.; Nan, Y.; Choi, S.; Liu, J.; Tavlarides, L. L.; Tsouris, C.; Yiacoumi, S. Capture of Iodine from Nuclear-Fuel-Reprocessing Off-Gas: Influence of Aging on a Reduced Silver Mordenite Adsorbent after Exposure to NO/NO_2. *ACS Appl. Mater. Interfaces* **2020**, *12* (44), 49680−49693.
(12) Asmussen, R. M.; Matyáš, J.; Qafoku, N. P.; Kruger, A. A. Silver-functionalized silica aerogels and their application in the removal of iodine from aqueous environments. *Journal of Hazardous Materials* **2019**, *379*, 119364.
(13) Chong, S.; Riley, B. J.; Kuang, W.; Olszta, M. J. Iodine Capture with Mechanically Robust Heat-Treated Ag-Al-Si-O Xerogel Sorbents. *ACS Omega* **2021**, *6* (17), 11628−11638.
(14) Riley, B. J.; Kroll, J. O.; Peterson, J. A.; Matyáš, J.; Olszta, M. J.; Li, X.; Vienna, J. D. Silver-Loaded Aluminosilicate Aerogels As Iodine Sorbents. *ACS Appl. Mater. Interfaces* **2017**, *9* (38), 32907−32919.
(15) Riley, B. J.; Chun, J.; Um, W.; Lepry, W. C.; Matyas, J.; Olszta, M. J.; Li, X.; Polychronopoulou, K.; Kanatzidis, M. G. Chalcogen-Based Aerogels As Sorbents for Radionuclide Remediation. *Environ. Sci. Technol.* **2013**, *47* (13), 7540−7547.
(16) Scott, S. M.; Hu, T.; Yao, T.; Xin, G.; Lian, J. Graphene-based sorbents for iodine-129 capture and sequestration. *Carbon* **2015**, *90* (C), 1−8.
(17) Li, B.; Dong, X.; Wang, H.; Ma, D.; Tan, K.; Jensen, S.; Deibert, B. J.; Butler, J.; Cure, J.; Shi, Z.; Thonhauser, T.; Chabal, Y. J.; Han, Y.; Li, J. Capture of organic iodides from nuclear waste by metal-organic framework-based molecular traps. *Nat. Commun.* **2017**, *8* (1), 485−485.
(18) McFarlane, J.; Riley, B. J.; Holcomb, D. E.; Lines, A.; Andrews, H. B.; Bryan, S. A.; Chapel, A. S.; Ezell, N. D. B.; Felmy, H. M.; Greenwood, M. S.; Humrickhouse, P. W.; Myhre, K. G. *Molten Salt Reactor Engineering Study for Off-Gas Management*, ORNL/TM-2020/1602, PNNL-30159, 2020.
(19) Andrews, H. B.; McFarlane, J.; Chapel, A. S.; Ezell, N. D. B.; Holcomb, D. E.; de Wet, D.; Greenwood, M. S.; Myhre, K. G.; Bryan, S. A.; Lines, A.; Riley, B. J.; Felmy, H. M.; Humrickhouse, P. W. Review of molten salt reactor off-gas management considerations. *Nucl. Eng. Des.* **2021**, *385*, 111529.
(20) Riley, B. J.; Vienna, J. D.; Strachan, D. M.; McCloy, J. S.; Jerden, J. L. Materials and processes for the effective capture and immobilization of radioiodine: A review. *J. Nucl. Mater.* **2016**, *470* (C), 307−326.
(21) Bruffey, S. H. S.; Strachan, D. M.; Jubin, R. T.; Soelberg, N. R.; Riley, B. J. *A literature Survey to Identify Potentially Voltaile Iodine-Bearing Species Present in Off-gas Streams, INL/EXT-15-35609*; Idaho National Laboratory: 2015.
(22) McFarlane, J.; Wren, J. C.; Lemire, R. J. Chemical Speciation of Iodine Source Term to Containment. *Nuclear Technology* **2002**, *138* (2), 162−178.
(23) Hughey, K. D.; Bradley, A. M.; Tonkyn, R. G.; Felmy, H. M.; Blake, T. A.; Bryan, S. A.; Johnson, T. J.; Lines, A. M. Absolute Band Intensity of the Iodine Monochloride Fundamental Mode for Infrared Sensing and Quantitative Analysis. *Journal of Physical Chemistry. A* **2020**, *124* (46), 9578−9588.
(24) Hughey, K. D.; Bradley, A. M.; Felmy, H. M.; Clifford, A. J.; Cox, R. M.; Lines, A. M.; Bryan, S. A.; Johnson, T. J. Quantitative far-infrared band strengths of iodine monochloride (ICl), a molten salt off-gas product. *SPIE* **2020**, *11416*, 114160−114168.
(25) Li, B.; Dong, X.; Wang, H.; Ma, D.; Tan, K.; Shi, Z.; Chabal, Y. J.; Han, Y.; Li, J. Functionalized metal organic frameworks for effective capture of radioactive organic iodides. *Faraday Discuss.* **2017**, *201*, 47−61.
(26) Saha, S.; Roy, S.; Mathi, P.; Mondal, J. A. Adsorption of Iodine Species (I^{3-}, I^-, and IO_3^-) at the Nuclear Paint Monolayer-Water Interface and Its Relevance to a Nuclear Accident Scenario. *Journal of Physical Chemistry. A* **2020**, *124* (33), 6726−6734.
(27) Epimakhov, V. N.; Moskvin, L. N.; Chetverikov, V. V.; Oleinik, M. S.; Mysik, S. G. Improvement of the Procedure for Monitoring Iodine Radionuclides in Off-Gases from Nuclear Power Facilities. *Radiochemistry* **2018**, *60* (3), 304−308.
(28) Otto, H. W.; Seward, R. P. Phase Equilibria in the Potassium Hydroxide-Sodium Hydroxide System. *J. Chem. Eng. Data* **1964**, *9* (4), 507−508.
(29) Liu, X.; Fechler, N.; Antonietti, M. Salt melt synthesis of ceramics, semiconductors and carbon nanostructures. *Chem. Soc. Rev.* **2013**, *42* (21), 8237−8265.
(30) Claes, P.; Mernier, F.; Wery, L.; Glibert, J. Composition dependence of the oxoacidobasic properties of molten hydroxides. *Electrochim. Acta* **1999**, *44* (23), 3999−4006.
(31) Clifford, A. J.; Lackey, H. E.; Nelson, G. L.; Bryan, S. A.; Lines, A. M. Raman Spectroscopy Coupled with Chemometric Analysis for Speciation and Quantitative Analysis of Aqueous Phosphoric Acid Systems. *Anal. Chem.* **2021**, *93* (14), 5890−5896.
(32) Lackey, H. E.; Nelson, G. L.; Lines, A. M.; Bryan, S. A. Reimagining pH Measurement: Utilizing Raman Spectroscopy for Enhanced Accuracy in Phosphoric Acid Systems. *Anal. Chem.* **2020**, *92* (8), 5882−5889.
(33) Lines, A. M.; Adami, S. R.; Sinkov, S. I.; Lumetta, G. J.; Bryan, S. A. Multivariate Analysis for Quantification of Plutonium(IV) in Nitric Acid Based on Absorption Spectra. *Anal. Chem.* **2017**, *89* (17), 9354−9359.
(34) Felmy, H. M.; Clifford, A. J.; Medina, A. S.; Cox, R. M.; Wilson, J. M.; Lines, A. M.; Bryan, S. A. On-Line Monitoring of Gas-Phase Molecular Iodine Using Raman and Fluorescence Spectroscopy Paired with Chemometric Analysis. *Environ. Sci. Technol.* **2021**, *55*, 3898−3908.
(35) Lines, A. M.; Hall, G. B.; Asmussen, S.; Allred, J.; Sinkov, S.; Heller, F.; Gallagher, N.; Lumetta, G. J.; Bryan, S. A. Sensor Fusion: Comprehensive Real-Time, On-Line Monitoring for Process Control via Visible, Near-Infrared, and Raman Spectroscopy. *ACS Sensors* **2020**, *5* (8), 2467−2475.
(36) Lines, A. M.; Hall, G. B.; Sinkov, S. I.; Levitskaia, T.; Gallagher, N. B.; Lumetta, G. J.; Bryan, S. A. Overcoming oxidation state dependent spectral interferences: On-line monitoring of U(VI) reduction to U(IV) via Raman and UV-vis spectroscopy. *Ind. Eng. Chem. Res.* **2020**, *59*, 8894−8901.
(37) Beghi, I.; Lind, T.; Prasser, H.-M. Experimental studies on retention of iodine in a wet scrubber. *Nucl. Eng. Des.* **2018**, *326*, 234−243.
(38) Trowbridge, L. D. *Molten Hydroxide Trapping Process for Radioiodine*; ORNL/TM--002/247; Oak Ridge National Laboratory (ORNL), Oak Ridge, TN, United States, 2003.
(39) Lines, A. M.; Nelson, G. L.; Casella, A. J.; Bello, J. M.; Clark, S. B.; Bryan, S. A. Multivariate Analysis To Quantify Species in the Presence of Direct Interferents: Micro-Raman Analysis of HNO3 in Microfluidic Devices. *Anal. Chem.* **2018**, *90* (4), 2548−2554.
(40) Schroll, C. A.; Lines, A. M.; Heineman, W. R.; Bryan, S. A. Absorption spectroscopy for the quantitative prediction of lanthanide concentrations in the 3LiCl-2CsCl eutectic at 723 K. *Anal Methods-Uk* **2016**, *8* (43), 7731−7738.

https://doi.org/10.1021/acsomega.2c05522
ACS Omega 2022, 7, 40456−40465

(41) Krishnamurti, D. The Raman and infra-red spectra of some solid hydroxides. *Proceedings of the Indian Academy of Sciences - Section A* **1959**, *50* (4), 232−246.
(42) Walrafen, G. E.; Douglas, R. T. W. Raman spectra from very concentrated aqueous NaOH and from wet and dry, solid, and anhydrous molten, LiOH, NaOH, and KOH. *J. Chem. Phys.* **2006**, *124* (11), 114504.
(43) Sherwood, P. M. A.; Turner, J. J. Vibrational spectra of compounds in the iodine pentoxide-water system and sodium iodate. *Spectrochimica Acta Part A: Molecular Spectroscopy* **1970**, *26* (10), 1975−1992.
(44) Maroni, V. A.; Hathaway, E. J. Laser raman studies of the iodate ion in molten nitrate solutions. *Journal of Inorganic and Nuclear Chemistry* **1972**, *34* (10), 3049−3053.
(45) Long, G. L.; Winefordner, J. D. Limit of Detection A Closer Look at the IUPAC Definition. *Anal. Chem.* **1983**, *55* (07), 712A−724A.
(46) Harris, D. C. *Quantitative chemical analysis*, 7th ed.; W.H. Freeman: 2007.
(47) Roy, S.; Wrzesinski, P. J.; Pestov, D.; Dantus, M.; Gord, J. R. Single-beam coherent anti-Stokes Raman scattering (CARS) spectroscopy of gas-phase CO2 via phase and polarization shaping of a broadband continuum. *J. Raman Spectrosc.* **2010**, *41* (10), 1194−1199.
(48) Lackey, H. E.; Colburn, H. A.; Olarte, M. V.; Lemmon, T.; Felmy, H. M.; Bryan, S. A.; Lines, A. M. On-Line Raman Measurement of the Radiation-Enhanced Reaction of Cellobiose with Hydrogen Peroxide. *ACS Omega* **2021**, *6* (51), 35457−35466.
(49) Hou, X. L.; Hansen, V.; Aldahan, A.; Possnert, G.; Lind, O. C.; Lujaniene, G. A review on speciation of iodine-129 in the environmental and biological samples. *Anal. Chim. Acta* **2009**, *632* (2), 181−196.
(50) Galica, G. E.; Johnson, B. R.; Kinsey, J. L.; Hale, M. O. Incident Frequency-Dependence and Polarization Properties of the Ch3i Raman-Spectrum. *J. Phys. Chem.* **1991**, *95* (21), 7994−8004.
(51) Markel, F.; Myers, A. B. Resonance Raman Excitation Profiles of Methyl-Iodide in Hexane. *J. Chem. Phys.* **1993**, *98* (1), 21−30.

https://doi.org/10.1021/acsomega.2c05522
ACS Omega 2022, 7, 40456−40465